

Tunable Dirac States in a Two-Dimensional Su-Schrieffer-Heeger Model

Chang-An Li,^{1,*} Sang-Jun Choi,¹ Song-Bo Zhang,² and Björn Trauzettel^{1,3}

¹*Institute for Theoretical Physics and Astrophysics,
University of Würzburg, 97074 Würzburg, Germany*

²*Department of Physics, University of Zürich, Winterthurerstrasse 190 8057, Zürich, Switzerland*

³*Würzburg-Dresden Cluster of Excellence ct.qmat, Germany*

(Dated: February 8, 2022)

We propose to realize Dirac states in a two-dimensional Su-Schrieffer-Heeger model on a square lattice. We show that a pair of Dirac points protected by space-time inversion symmetry appear in the semimetal phase. Remarkably, the locations of these Dirac points are *not* pinned to any high-symmetry points of the Brillouin zone but highly tunable through parameter modulations. Moreover, the merging of two Dirac points undergoes a novel topological phase transition, which leads to either a weak topological insulator or a nodal-line semimetal. We provide a systematic analysis of these topological phases from both bulk and boundary perspectives combined with symmetry arguments. We also discuss feasible experimental platforms to realize our model.

Introduction.— Two-dimensional (2D) massless Dirac states have attracted tremendous attention in condensed matter physics and material science since the successful realization of graphene [1–5]. The Dirac states in graphene exhibit particular transport properties such as anomalous quantum Hall effect [6], minimum conductivity [7, 8], and Klein tunneling [9, 10]. Since the large momentum separation of Dirac points guarantees two independent valley degrees of freedom, graphene provides many interesting applications such as valley filters [11] and valleytronics [12, 13]. Nevertheless, possible variations of the momentum separation and effective velocities of Dirac points change the transport properties significantly because of corresponding variations of intervalley scattering and density of states. For instance, the intervalley scattering can give rise to a crossover from weak antilocalization to localization in transport [14–16]. However, Dirac points in graphene are pinned to the corners of the hexagonal Brillouin zone (BZ) by C_{3v} group symmetry of the honeycomb lattice. They can only be slightly shifted by applying external strain [17]. Therefore, searching for alternative graphene-like 2D platforms that host Dirac states with conveniently tunable properties is of fundamental importance and interest.

In this work, we propose to realize 2D Dirac states with highly tunable properties on a Su-Schrieffer-Heeger (SSH) square lattice. Recently, research activities related to the generalization of the SSH model [18] to 2D have attracted broad interest [19–21] and sparked the fast-expanding field of higher-order topological insulators [22–34]. In our proposal, we consider a 2D SSH model with alternately dimerized patterns [Fig. 1(a)]. Astonishingly, we find that such a 2D SSH model hosts massless Dirac states in the BZ in a broad parameter range [Figs. 1(b,d)]. We show that the Dirac points are protected by a space-time inversion symmetry. Remarkably, the locations of Dirac points are highly tunable by hopping parameters [Fig. 1(c)]. In contrast to graphene, the merging of the two Dirac points in our model experience

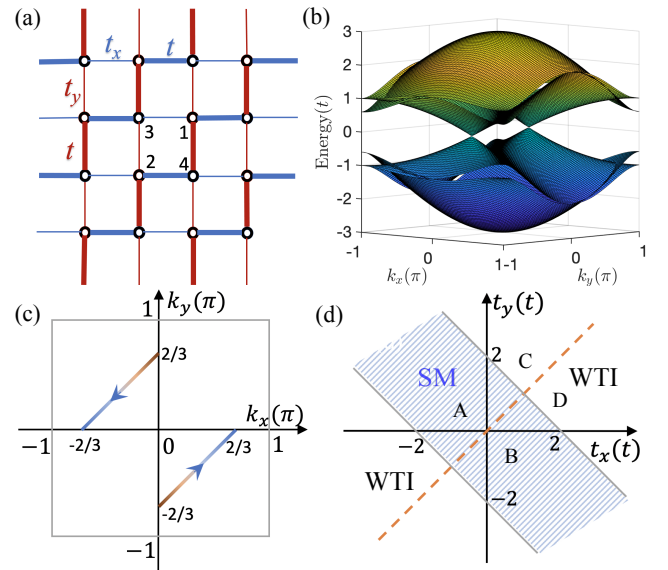


Figure 1. (a) Schematic of the inclined 2D SSH lattice. Blue (red) thick and thin bonds mark alternately dimerized hopping strengths in $x(y)$ -direction. (b) Band structure of the inclined 2D SSH model with a pair of Dirac points. Here, we take $t_x = 0.2t$ and $t_y = 0.8t$. (c) Moving pattern of the pair of Dirac points corresponding to the condition in Eq. (4). (d) Phase diagram of the inclined 2D SSH model in the (t_x, t_y) parameter space. The shadowed region (excluding the orange dashed line) represents the semimetal (SM) with a pair of Dirac points. The orange dashed line at $t_x = t_y$ corresponds to the nodal-line semimetal. Other regions denote the weak topological insulator (WTI) regime. The four points A, B, C, and D label the representative phase points that we refer to in the text.

a particular topological phase transition resulting in interesting phases, i.e., either a weak topological insulator or a nodal-line semimetal [Fig. 1(d)]. We demonstrate the topological origin of these different phases by employing two independent winding numbers together with boundary signatures and symmetry arguments. We also

discuss how to realize our model experimentally based on synthetic quantum materials.

Inclined two-dimensional Su-Schrieffer-Heeger model.–

We consider a particular 2D SSH model, as shown in Fig. 1(a), where the weak (thin) bonds and strong (thick) bonds are alternately dimerized along the two adjacent parallel lattice rows (x -direction) or columns (y -direction). We call it the inclined 2D SSH model. There are four orbital degrees of freedom in each unit cell (labeled as 1–4). We consider spinless fermions, for clarity. The effective Bloch Hamiltonian describing the inclined 2D SSH model in reciprocal space reads

$$H(\mathbf{k}) = \begin{pmatrix} 0 & q \\ q^\dagger & 0 \end{pmatrix}, q(\mathbf{k}) \equiv \begin{pmatrix} t_x + te^{ik_x} & t + t_y e^{ik_y} \\ t_y + te^{-ik_y} & t + t_x e^{-ik_x} \end{pmatrix}, \quad (1)$$

where $\mathbf{k} = (k_x, k_y)$ is the 2D wave-vector; t and $t_{x/y}$ are the staggered hopping amplitudes along x/y -directions. Without loss of generality, we set the lattice constant to be unity and assume $t > 0$ hereafter. The basis is $(\Psi_{\mathbf{k}1}, \Psi_{\mathbf{k}2}, \Psi_{\mathbf{k}3}, \Psi_{\mathbf{k}4})$ of Bloch states constructed on the four sites of the unit cell. The Hamiltonian in Eq. (1) respects chiral (sublattice) symmetry, as indicated by its block off-diagonal form. Explicitly, the chiral symmetry yields $\mathcal{C}H(\mathbf{k})\mathcal{C}^{-1} = -H(\mathbf{k})$ with the chiral-symmetry operator $\mathcal{C} = \tau_3 \otimes \sigma_0$, where τ and σ are Pauli matrices for different orbital degrees of freedom in the unit cell. The energy bands of Eq. (1) are obtained as

$$E_\eta^\pm(\mathbf{k}) = \pm \sqrt{\xi_\eta^2(\mathbf{k}) + \zeta_\eta^2(\mathbf{k})} = \pm |\varepsilon_\eta(\mathbf{k})|, \quad (2)$$

where $\xi_\eta(\mathbf{k}) \equiv (t + t_x) \cos \frac{k_x}{2} + \eta(t + t_y) \cos \frac{k_y}{2}$, $\zeta_\eta(\mathbf{k}) \equiv (t - t_x) \sin \frac{k_x}{2} - \eta(t - t_y) \sin \frac{k_y}{2}$, and $\varepsilon_\eta(\mathbf{k}) \equiv \xi_\eta(\mathbf{k}) + i\zeta_\eta(\mathbf{k})$ with $\eta = \pm 1$. Note that even though Eq. (1) cannot be expressed in terms of anticommutating Dirac matrices only, its energy spectrum still has the corresponding form, i.e., a square root of the summation of some squared variables.

Highly tunable Dirac states on square lattices.– A pair of Dirac points appear in the BZ of the inclined 2D SSH model, as shown in Fig. 1(b). Astonishingly, the Dirac points are not pinned to high-symmetry points but are highly tunable by parameter modulations. To elucidate this property, it is instructive to obtain their locations analytically. Due to the presence of chiral symmetry, the conduction and valence bands touch at zero energy. Thus, the existence of Dirac points yields the conditions $\xi_\eta(\mathbf{k}) = \zeta_\eta(\mathbf{k}) = 0$. Solving these condition equations, we find a pair of Dirac points located at $\mathbf{K}_\pm \equiv \pm(K_x, -K_y)$, where $K_{x/y}$ are given by

$$K_{x/y} = 2 \arccos \sqrt{\frac{(t + t_{y/x})^2 (2t - t_x - t_y)}{4t(t^2 - t_x t_y)}}. \quad (3)$$

From Eq. (3), we find that a physical solution (with real $K_{x/y}$ that corresponds to the presence of Dirac points)

only holds when $|t_x + t_y| < 2t$ and $t_x \neq t_y$. The full phase diagram of the inclined 2D SSH model is illustrated in Fig. 1(d) and will be discussed in more detail later.

Clearly, our model exhibits two Dirac points whose locations are highly tunable. To show this feature more explicitly, we consider a simple parameterization with $t_x = s \in [0, t]$, $t_y = t - s$, and $t = 1$. Then, we find the relation

$$K_x + K_y = 2\pi/3. \quad (4)$$

As a result, the Dirac points move along a line segment when we vary the parameter s , as shown in Fig. 1(c). Interestingly, no symmetries are broken as we move around Dirac points by variation of t_x and t_y . Moreover, the effective Fermi velocity around the Dirac points in our model can also be manipulated by parameter modulations.

Space-time inversion symmetry protection.– In the unperturbed case with chiral symmetry, the Dirac points are topologically described by a quantized charge $Q_{\mathbf{K}_\pm} = \frac{1}{2\pi i} \oint_\ell d\mathbf{k} \cdot \text{Tr} [q^{-1}(\mathbf{k}) \nabla_{\mathbf{k}} q(\mathbf{k})]$ [35–38], where the loop ℓ is chosen such that it encircles a single Dirac point \mathbf{K}_\pm . The two Dirac points in the BZ have opposite topological charges $Q_{\mathbf{K}_\pm} = \pm 1$. They annihilate each other when they meet in \mathbf{k} -space. In a more general sense, the stability of the Dirac points in our model is protected by a space-time inversion symmetry which is composed of an inversion symmetry and time-reversal symmetry [39, 40]. Note that due to the alternate dimerization along adjacent two lattice rows or columns, the usual inversion symmetry is broken. If we, however, perform a glide operation (half-unit translation) followed by an inversion operation, then the system goes back to itself. We term this symmetry as “glide-inversion” symmetry. Explicitly, the glide-inversion symmetry requires

$$\mathcal{G}_I^{x,y}(\mathbf{k}) H(\mathbf{k}) [\mathcal{G}_I^{x,y}(\mathbf{k})]^{-1} = H(-\mathbf{k}), \quad (5)$$

where $\mathcal{G}_I^{x,y}(\mathbf{k}) = I \times g_{x/y}$, $I = \tau_0 \otimes \sigma_1$ is the conventional inversion operator, $g_x = \tau_1 \otimes \begin{pmatrix} e^{ik_x} & 0 \\ 0 & 1 \end{pmatrix}$ and $g_y = \tau_1 \otimes \begin{pmatrix} 0 & e^{ik_y} \\ 1 & 0 \end{pmatrix}$ are half-unit translations along x - and y -directions, respectively. Note that this glide-inversion symmetry can be equivalently viewed as inversion symmetry with the inversion center shifted to the bond center of each unit cell [see Fig. 1(a)], we still keep the term “glide-inversion” to indicate its \mathbf{k} -dependence clearly. In addition, the system respects spinless time-reversal symmetry, i.e., $\mathcal{T}H(\mathbf{k})\mathcal{T}^{-1} = H(-\mathbf{k})$, where the time-reversal symmetry operator is given by the complex conjugation $\mathcal{T} = \mathcal{K}$. Thus, the space-time inversion operator can be written as $\mathcal{S} = \mathcal{G}_I^{x,y}(\mathbf{k})\mathcal{T} = \tau_0 \otimes \sigma_1 \times g_{x/y}\mathcal{K}$. It is a local operation in \mathbf{k} -space,

$$\mathcal{S}H(\mathbf{k})\mathcal{S}^{-1} = H(\mathbf{k}), \quad \mathcal{S}^2 = 1. \quad (6)$$

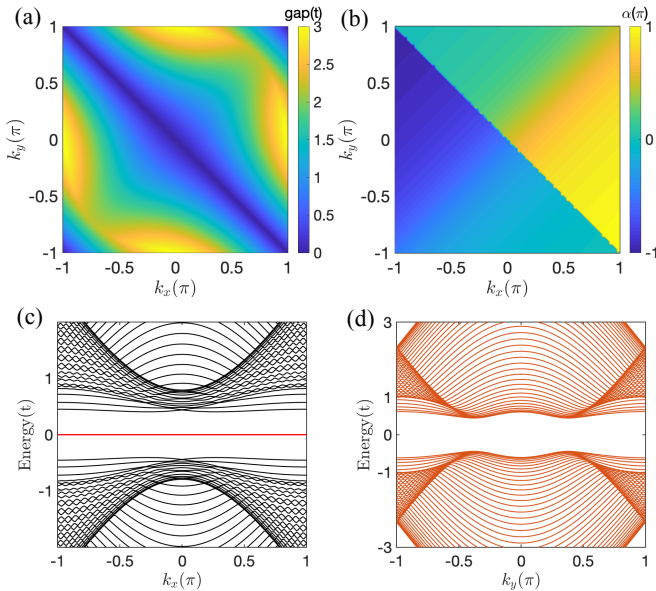


Figure 2. (a) Energy gap in the whole BZ for $t_x = t_y = 0.5$. A gapless nodal line appears at the line $k_x + k_y = 0$. (b) Angle $\alpha \equiv \arg[\varepsilon_{\eta=+1}(\mathbf{k})]$ in the BZ for $t_x = t_y = 0.5$. There is a branch cut at the line $k_x + k_y = 0$. (c) Energy spectrum of a ribbon along x -direction with width $W_y = 20$. Notice the flat band at zero energy. (d) Energy spectrum of the ribbons along y -direction with width $W_x = 20$. Here we choose $t_x = 1.2t, t_y = 1.8t$ such that $w_x = 0, w_y = 1$.

Under the constraint of \mathcal{S} , the Berry curvature is zero at every point in the BZ except at the Dirac points [39, 40]. Hence, the quantized π Berry phase around a Dirac point protects its stability. Indeed, if we add a staggered onsite potential as a perturbation, say $\Delta\tau_3\sigma_0$ with Δ indicating its strength, to break the glide-inversion symmetry, the Dirac points are removed and a bulk gap opens [38]. If we, however, consider another type of staggered onsite potential $\Delta\tau_0\sigma_3$, which breaks chiral symmetry, while it respects glide-inversion symmetry, then the Dirac points remain intact [38]. Therefore, the π Berry phase is the main topological quantity that protects the Dirac points in our model since the chiral topological charge $Q_{\mathbf{K}_{\pm}}$ needs the chiral symmetry to be well-defined.

Topological phase transitions with merging of Dirac points.— The mergence of two Dirac points undergoes a topological phase transition in our model. The semimetal phase with a pair of Dirac points locates in the shadowed region $|t_x + t_y| < 2t$ and $t_x \neq t_y$ of Fig. 1(d). The topological phase transition after merging a pair of Dirac points transforms the semimetal phase to either a weak topological insulator or a nodal-line semimetal. Thus, our inclined 2D SSH model actually possesses three different topological phases, as shown in the phase diagram in Fig. 1(d). Let us first focus on the nodal-line semimetal phase under the specific condition $t_x = t_y$ [Fig. 1(d) and Fig. 2(a)]. Consider a representative phase point A (or B) in

the semimetal phase with a pair of Dirac points [see Fig. 1(d)]. As it moves towards the orange line, the Dirac points merge and we observe that the system exhibits a gapless nodal line at

$$k_x + k_y = 0, \text{ if } t_x = t_y \neq t, \quad (7)$$

The appearance of a gapless nodal line is a direct consequence of an accidental mirror symmetry [38]. This special symmetry, together with chiral symmetry, enforces the degeneracy at $E = 0$ on the line $k_x + k_y = 0$.

The nodal-line semimetal phase is protected by a topological invariant δ as we describe below. Let us define the angle α as $\alpha(\mathbf{k}) \equiv \arg[\varepsilon_{\eta=+1}(\mathbf{k})]$ where $\varepsilon_{\eta}(\mathbf{k})$ is defined below Eq. (2). In the nodal-line semimetal phase, $\varepsilon_{\eta=+1}(\mathbf{k}) = (t + t_x)(\cos \frac{k_x}{2} - \cos \frac{k_y}{2}) + i(t - t_x)(\sin \frac{k_x}{2} + \sin \frac{k_y}{2})$. Figure 2(b) shows the angle α in the BZ in the nodal-line semimetal phase. The branch cut at $k_x + k_y = 0$ separates the BZ into two equal sections. Thus, the topological invariant δ can be defined as $\delta \equiv (\text{sgn}[\alpha(\mathbf{k}_1)] - \text{sgn}[\alpha(\mathbf{k}_2)])/2 \bmod 2$, where the wavevectors \mathbf{k}_1 and \mathbf{k}_2 are located on the two different sections separated by the nodal-line. In the case of Figs. 2(a) and 2(b), it is found that $\delta = 1$.

Again, we consider a representative phase point A (or B) in the semimetal phase in Fig. 1(d). As it moves parallel to the orange line, two Dirac points merge at the phase boundary $|t_x + t_y| = 2t$. Similar to the case of graphene, the energy spectrum stays linear along one direction while it becomes parabolic along another direction at the critical merging points [41]. This topological phase transition gives rise to a weak topological insulator rather than a trivial insulator (see the representative phase point C and D). The weak topological insulators are located in the region $|t_x + t_y| > 2t$ and $t_x \neq t_y$. They are described by two winding numbers (w_x, w_y) with one of them being one and the other one being zero. The winding number is defined as $w_{x/y} = \frac{1}{2\pi i} \int_0^{2\pi} dk_{x/y} \text{Tr}[q^{-1}(\mathbf{k})\partial_{k_{x/y}}q(\mathbf{k})]$ for arbitrary $k_{x/y} \in [0, 2\pi]$. When $w_x = 1, w_y = 0$ ($w_x = 0, w_y = 1$), the system is nontrivial along x (y)-direction and trivial along y (x)-direction. Actually, this anisotropic topological insulating phase can be further divided into two subphases: (i) $w_x = 1, w_y = 0$ ($t_x > t_y$ and $|t_x + t_y| > 2t$) and (ii) $w_x = 0, w_y = 1$ ($t_x < t_y$ and $|t_x + t_y| > 2t$). Correspondingly, a totally flat edge band exists in the gap of the energy spectrum along x (y)-direction for the subphase (i) (subphase (ii)) [see, for instance, Fig. 2(c)]. Notably, neither the topologically trivial phase with $w_x = w_y = 0$ nor the topologically nontrivial phase with $w_x = w_y = 1$ appear in the inclined 2D SSH model.

Anisotropic projection of Dirac points.— The projection of two Dirac points to different directions shows two patterns as illustrated in Figs. 3(a) and 3(b). These two patterns can be described by the representative phase points A and B in Fig. 1(d), respectively. To switch between

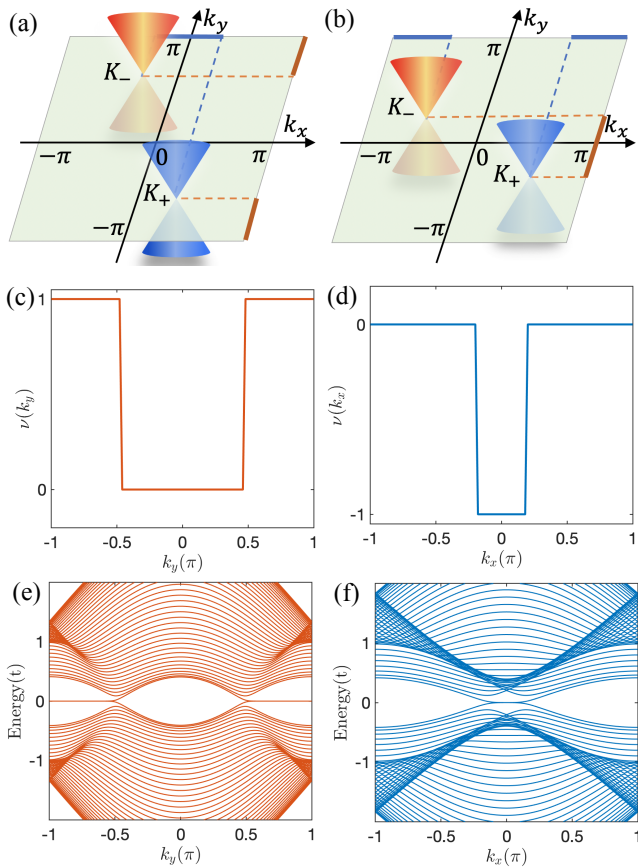


Figure 3. Anisotropic projection of the two Dirac points. (a) Schematic of anisotropic projection of bulk spectrum with two Dirac points (\mathbf{K}_{\pm}) to x - and y -directions under the condition $t_x < t_y$. The dashed lines represent the projection direction. The thick solid lines (blue and red) at the boundary of the BZ indicate the nontrivial regions with flat edge bands. (b) Alternative projection similar to the case in (a) but under the condition $t_x > t_y$. (c) Winding number $\nu(k_y)$ as a function of k_y . (d) Winding number $\nu(k_x)$ as a function of k_x . (e) Energy spectrum of a ribbon along y -direction with width $W_x = 20$ corresponding to the case in panel (c). Notice the flat band at zero energy. (f) Energy spectrum of the ribbons along x -direction with width $W_y = 20$ corresponding to the the case in panel (d). In panels (c,d,e,f), the other parameters are $t_x = 0.3t$ and $t_y = 0.7t$, i.e., corresponding to the case in (a).

the two possible patterns, a phase point has to cross the gapless nodal-line semimetal phase. For simplicity, let us focus on the pattern in Fig. 3(a). When projecting the system along $x(y)$ -direction, the same region in the BZ can be viewed as topologically nontrivial or trivial depending on relative values of t_x and t_y [see, for instance, Fig. 3(a) for $t_x < t_y$]. This anisotropic nature in our model suggests two independent indexes $\nu(k_x)$ and $\nu(k_y)$. Explicitly, they are given by

$$\nu(k_{x/y}) = \frac{1}{2\pi} \int_0^{2\pi} dk_{y/x} \frac{t^2 e^{\mp i k_{y/x}} - t_{y/x}^2 e^{\pm i k_{y/x}}}{R(\mathbf{k})}, \quad (8)$$

where $R(\mathbf{k}) \equiv (t e^{i k_x/2} + t_x e^{-i k_x/2})^2 - (t e^{-i k_y/2} + t_y e^{i k_y/2})^2$. In essence, $\nu(k_{x/y})$ is a winding number of the reduced one-dimensional system at specific wave-number $k_{x/y}$ [42, 43]. In Fig. 3(c), the middle region is trivial ($\nu = 0$) while the two outer regions are nontrivial ($\nu = 1$). It is interesting to see that this pattern is in stark contrast to that of Fig. 3(d), i.e., $\nu = -1$ in the middle region and $\nu = 0$ otherwise. This difference comes from the anisotropic nature of the alternating dimerization pattern in our system. The nontrivial winding number indicates the existence of flat edge bands at open boundaries [42–45]. Evidently, the regions of flat bands in Figs. 3(e) and 3(f) agree with the topological nontrivial regions in Figs. 3(c) and 3(d), respectively.

Discussion and conclusion.— To realize our 2D SSH model experimentally, it needs a square lattice geometry (four sites in a unit cell) and controllable nearest-neighbor couplings. Required techniques for designing such a lattice structure have been developed in synthetic quantum materials such as photonic and acoustic crystals [26–28, 46, 47], electric circuits [25], and waveguides [29, 48]. For instance, to realize our model in a photonic waveguide system, waveguides can be arranged to a square lattice with four waveguides contained in each unit cell and the alternately dimerized couplings between neighboring waveguides can be modulated by their spacings [48, 49]. Notably, our 2D SSH model does not require delicate manipulations of external flux. Another feasible platform to realize our model is based on ultracold gases in optical lattices [50, 51], in which the lattice geometry and hopping strengths are adjustable.

Our model has a richer topological phase space accompanied with corresponding topological phase transitions as compared with a honeycomb lattice formed by ultracold gases [51]. Moreover, the realization of our model on a square lattice is much simpler as the Mielke checkerboard model [52] since it only involves nearest-neighbor hopping terms. We emphasize that our results are distinctively different from recent reports to realize Dirac states on square lattices [53–55]. These proposals require external π fluxes, and the Dirac points are pinned to boundaries of the BZ. In our model, the two valley degrees of freedom in \mathbf{k} -space can be conveniently controlled. Therefore, it may provide potential applications in valley-based electronics. Interestingly, our model even may provide a platform to realize the so called toric-code insulator [56].

In conclusion, we have proposed a 2D SSH model on a square lattice to realize highly tunable Dirac states. We have found that the locations of Dirac points are not pinned to any high-symmetry points or lines in the BZ but movable by parameter modifications. The mergence of two Dirac points leads to a topological phase transition, which converts the system from a semimetal phase with a pair of Dirac points to either a weak topological insulator or a nodal-line semimetal. We expect that

our model can be realized in different metamaterial platforms.

This work was supported by the DFG (SPP1666 and SFB1170 “ToCoTronics”), the WÄErzburg-Dresden Cluster of Excellence ct.qmat, EXC2147, Project-id 390858490, the Elitenetzwerk Bayern Graduate School on “Topological Insulators”, and the High Tech Agenda Bayern.

* changan.li@uni-wuerzburg.de

- [1] K. S. Novoselov, A. K. Geim, S. V. Morozov, D. Jiang, M. I. Katsnelson, I. V. Grigorieva, S. V. Dubonos, and A. A. Firsov, *Nature* **438**, 197 (2005).
- [2] A. H. Castro Neto, F. Guinea, N. M. R. Peres, K. S. Novoselov, and A. K. Geim, *Rev. Mod. Phys.* **81**, 109 (2009).
- [3] C.-C. Liu, W. Feng, and Y. Yao, *Phys. Rev. Lett.* **107**, 076802 (2011).
- [4] D. Malko, C. Neiss, F. Viñes, and A. Görling, *Phys. Rev. Lett.* **108**, 086804 (2012).
- [5] S. M. Young and C. L. Kane, *Phys. Rev. Lett.* **115**, 126803 (2015).
- [6] Y. Zhang, Y.-W. Tan, H. L. Stormer, and P. Kim, *Nature* **438**, 201 (2005).
- [7] T. Ando, Y. Zheng, and H. Suzuura, *J. Phys. Soc. Jap.* **71**, 1318 (2002).
- [8] J. Tworzydło, B. Trauzettel, M. Titov, A. Rycerz, and C. W. J. Beenakker, *Phys. Rev. Lett.* **96**, 246802 (2006).
- [9] M. I. Katsnelson, K. S. Novoselov, and A. K. Geim, *Nat Phys* **2**, 620 (2006).
- [10] N. Stander, B. Huard, and D. Goldhaber-Gordon, *Phys. Rev. Lett.* **102**, 026807 (2009).
- [11] A. Rycerz, J. Tworzydło, and C. W. J. Beenakker, *Nature Physics* **3**, 172 (2007).
- [12] D. Xiao, W. Yao, and Q. Niu, *Phys. Rev. Lett.* **99**, 236809 (2007).
- [13] W. Yao, D. Xiao, and Q. Niu, *Phys. Rev. B* **77**, 235406 (2008).
- [14] H. Suzuura and T. Ando, *Phys. Rev. Lett.* **89**, 266603 (2002).
- [15] A. F. Morpurgo and F. Guinea, *Phys. Rev. Lett.* **97**, 196804 (2006).
- [16] E. McCann, K. Kechedzhi, V. I. Fal’ko, H. Suzuura, T. Ando, and B. L. Altshuler, *Phys. Rev. Lett.* **97**, 146805 (2006).
- [17] V. M. Pereira, A. H. Castro Neto, and N. M. R. Peres, *Phys. Rev. B* **80**, 045401 (2009).
- [18] W. P. Su, J. R. Schrieffer, and A. J. Heeger, *Phys. Rev. Lett.* **42**, 1698 (1979).
- [19] F. Liu and K. Wakabayashi, *Phys. Rev. Lett.* **118**, 076803 (2017).
- [20] W. A. Benalcazar, B. A. Bernevig, and T. L. Hughes, *Science* **357**, 61 (2017).
- [21] W. A. Benalcazar, B. A. Bernevig, and T. L. Hughes, *Phys. Rev. B* **96**, 245115 (2017).
- [22] Z. Song, Z. Fang, and C. Fang, *Phys. Rev. Lett.* **119**, 246402 (2017).
- [23] F. Schindler, A. M. Cook, M. G. Vergniory, Z. Wang, S. S. P. Parkin, B. A. Bernevig, and T. Neupert, *Science Advances* **4** (2018).
- [24] F. Schindler, Z. Wang, M. G. Vergniory, A. M. Cook, A. Murani, S. Sengupta, A. Y. Kasumov, R. Deblock, S. Jeon, I. Drozdov, H. Bouchiat, S. Guéron, A. Yazdani, B. A. Bernevig, and T. Neupert, *Nat. Phys.* **14**, 918 (2018).
- [25] S. Imhof, C. Berger, F. Bayer, J. Brehm, L. W. Molenkamp, T. Kiessling, F. Schindler, C. H. Lee, M. Greiter, T. Neupert, and R. Thomale, *Nat. Phys.* **14**, 925 (2018).
- [26] M. Serra-Garcia, V. Peri, R. Süsstrunk, O. R. Bilal, T. Larsen, L. G. Villanueva, and S. D. Huber, *Nature* **555**, 342 (2018).
- [27] B.-Y. Xie, G.-X. Su, H.-F. Wang, H. Su, X.-P. Shen, P. Zhan, M.-H. Lu, Z.-L. Wang, and Y.-F. Chen, *Phys. Rev. Lett.* **122**, 233903 (2019).
- [28] X.-D. Chen, W.-M. Deng, F.-L. Shi, F.-L. Zhao, M. Chen, and J.-W. Dong, *Phys. Rev. Lett.* **122**, 233902 (2019).
- [29] C. W. Peterson, W. A. Benalcazar, T. L. Hughes, and G. Bahl, *Nature* **555**, 346 (2018).
- [30] R.-X. Zhang, F. Wu, and S. Das Sarma, *Phys. Rev. Lett.* **124**, 136407 (2020).
- [31] C.-A. Li, B. Fu, Z.-A. Hu, J. Li, and S.-Q. Shen, *Phys. Rev. Lett.* **125**, 166801 (2020).
- [32] Q. Wei, X. Zhang, W. Deng, J. Lu, X. Huang, M. Yan, G. Chen, Z. Liu, and S. Jia, *Phys. Rev. Lett.* **127**, 255501 (2021).
- [33] S.-B. Zhang and B. Trauzettel, *Phys. Rev. Research* **2**, 012018 (2020).
- [34] C.-A. Li, S.-B. Zhang, J. Li, and B. Trauzettel, *Phys. Rev. Lett.* **127**, 026803 (2021).
- [35] A. P. Schnyder, S. Ryu, A. Furusaki, and A. W. W. Ludwig, *Phys. Rev. B* **78**, 195125 (2008).
- [36] A. P. Schnyder and S. Ryu, *Phys. Rev. B* **84**, 060504 (2011).
- [37] T. T. Heikkilä, N. B. Kopnin, and G. E. Volovik, *JETP Letters* **94**, 233 (2011).
- [38] See Supplemental Material at URL for details of the energy spectrum, the topological charge, the two-band effect model, the symmetry properties, and the phase diagram of the inclined 2D SSH model.
- [39] C. Fang and L. Fu, *Phys. Rev. B* **91**, 161105 (2015).
- [40] J. Kim, S. S. Baik, S. W. Jung, Y. Sohn, S. H. Ryu, H. J. Choi, B.-J. Yang, and K. S. Kim, *Phys. Rev. Lett.* **119**, 226801 (2017).
- [41] G. Montambaux, F. Piéchon, J.-N. Fuchs, and M. O. Goerbig, *Phys. Rev. B* **80**, 153412 (2009).
- [42] S.-Q. Shen, C.-A. Li, and Q. Niu, *2D Materials* **4**, 035014 (2017).
- [43] C.-A. Li, *J. Phys.: Condens. Matter* **32**, 025301 (2019).
- [44] S. Ryu and Y. Hatsugai, *Phys. Rev. Lett.* **89**, 077002 (2002).
- [45] P. Delplace, D. Ullmo, and G. Montambaux, *Phys. Rev. B* **84**, 195452 (2011).
- [46] Z. Wang, Y. Chong, J. D. Joannopoulos, and M. Soljačić, *Nature* **461**, 772 (2009).
- [47] X. Ni, M. Weiner, A. Alù, and A. B. Khanikaev, *Nat. Mater.* **18**, 113 (2019).
- [48] A. Cerjan, M. Jürgensen, W. A. Benalcazar, S. Mukherjee, and M. C. Rechtsman, *Phys. Rev. Lett.* **125**, 213901 (2020).
- [49] A. El Hassan, F. K. Kunst, A. Moritz, G. Andler, E. J. Bergholtz, and M. Bourennane, *Nat. Photonics* **13**, 697

- (2019).
- [50] G. Christian and B. Immanuel, *Science* **357**, 995 (2017).
- [51] L. Tarruell, D. Greif, T. Uehlinger, G. Jotzu, and T. Esslinger, *Nature* **483**, 302 (2012).
- [52] A. Mielke, *Journal of Physics A: Mathematical and General* **25**, 4335 (1992).
- [53] H. Xue, Z. Wang, Y.-X. Huang, Z. Cheng, L. Yu, Y. X. Foo, Y. X. Zhao, S. A. Yang, and B. Zhang, (2021), arXiv:2107.11564 [cond-mat.mes-hall].
- [54] T. Li, J. Du, Q. Zhang, Y. Li, X. Fan, F. Zhang, and C. Qiu, (2021), arXiv:2107.14579 [cond-mat.mes-hall].
- [55] L. B. Shao, Q. Liu, R. Xiao, S. A. Yang, and Y. X. Zhao, *Phys. Rev. Lett.* **127**, 076401 (2021).
- [56] P. M. Tam, J. W. F. Venderbos, and C. L. Kane, *Phys. Rev. B* **105**, 045106 (2022).

Supplemental material for “Tunable Dirac States in a Two-Dimensional Su-Schrieffer-Heeger Model”

Appendix S1: Properties of the inclined 2D SSH model

In this section, we present the band structure and phase diagram of the inclined 2D Su-Schrieffer-Heeger (SSH) model in the clean limit.

A. Model

We consider a 2D SSH model as shown in Fig. 1(a) of the main text. Here the weak (thin bonds) and strong (thick bonds) are alternately dimerized along the two adjacent parallel lattice rows (x -direction) or columns (y -direction). There are four orbital degrees of freedom in each unit cell (labeled as 1–4). The effective Bloch Hamiltonian describing such a 2D SSH model in reciprocal space reads

$$H(\mathbf{k}) = \begin{pmatrix} 0 & q(\mathbf{k}) \\ q^\dagger(\mathbf{k}) & 0 \end{pmatrix}; \quad q(\mathbf{k}) \equiv \begin{pmatrix} t_x + te^{ik_x} & t + t_y e^{ik_y} \\ t_y + te^{-ik_y} & t + t_x e^{-ik_x} \end{pmatrix} \quad (\text{S1.1})$$

Here, $\mathbf{k} = (k_x, k_y)$ is the 2D wave-vector; t and $t_{x/y}$ are the staggered hopping strengths along x/y directions. Without loss of generality, we set the lattice constant to be unity and assume $t > 0$. The basis for the Hamiltonian is $(\Psi_{\mathbf{k}1}, \Psi_{\mathbf{k}2}, \Psi_{\mathbf{k}3}, \Psi_{\mathbf{k}4})$ of Bloch states constructed on the four sites of a unit cell. Clearly, the Hamiltonian in Eq. (S1.1) respects chiral (sublattice) symmetry, as indicated by its block off-diagonal form. Explicitly, the chiral symmetry yields $\mathcal{C}H(\mathbf{k})\mathcal{C}^{-1} = -H(\mathbf{k})$ with the chiral-symmetry operator $\mathcal{C} = \tau_3 \otimes \sigma_0$, where τ and σ are Pauli matrices for different orbital degrees of freedom in a unit cell.

B. Eigen energy and eigen states

Let us calculate the spectrum of Eq. (S1.1). To do so, we utilize the general properties of the chiral symmetry. In the proper space, the chiral symmetry can be expressed as $\tau_3 H(\mathbf{k}) \tau_3 = -H(\mathbf{k})$. If we consider the eigen equation

$$H(\mathbf{k})\Psi_n = E_n\Psi_n, \quad \Psi_n = \frac{1}{\sqrt{2}} \begin{pmatrix} \psi_n^A \\ \psi_n^B \end{pmatrix},$$

where ψ_n^A and ψ_n^B are the states referring to A and B sublattices, respectively, then, due to the chiral symmetry, there is another state

$$\mathcal{C}\Psi_n = \begin{pmatrix} \psi_n^A \\ -\psi_n^B \end{pmatrix},$$

satisfying the eigen equation $H(\mathbf{k})[\mathcal{C}\Psi_n] = -E_n[\mathcal{C}\Psi_n]$. Squaring the Hamiltonian $H(\mathbf{k})$, this yields

$$H^2(\mathbf{k})\Psi_n = E_n^2\Psi_n.$$

Explicitly, we effectively decouple the equation as

$$\begin{aligned} h_A \psi_n^A &= E_n^2 \psi_n^A, & h_A &\equiv q(\mathbf{k})q^\dagger(\mathbf{k}), \\ h_B \psi_n^B &= E_n^2 \psi_n^B, & h_B &\equiv q^\dagger(\mathbf{k})q(\mathbf{k}). \end{aligned}$$

Note that $q(\mathbf{k})$ is not necessarily Hermitian, while the two defined operators h_A and h_B are Hermitian.

For our model, we obtain

$$h_A(\mathbf{k}) = h_0(\mathbf{k})\sigma_0 + h_1(\mathbf{k}) \begin{pmatrix} 0 & e^{i\frac{k_x+k_y}{2}} \\ e^{-i\frac{k_x+k_y}{2}} & 0 \end{pmatrix}, \quad (\text{S1.2})$$

$$h_0(\mathbf{k}) = t^2 + 2t_x t \cos k_x + t_x^2 + t^2 + 2t_y t \cos k_y + t_y^2, \quad (\text{S1.3})$$

$$h_1(\mathbf{k}) = 2 \left[(t+t_x)(t+t_y) \cos \frac{k_x}{2} \cos \frac{k_y}{2} - (t-t_x)(t-t_y) \sin \frac{k_x}{2} \sin \frac{k_y}{2} \right]. \quad (\text{S1.4})$$

Thus, the energy of the system is

$$\begin{aligned} E_\eta^\pm &= \pm \sqrt{h_0(\mathbf{k}) + \eta h_1(\mathbf{k})} \\ &= \pm \sqrt{\left[(t+t_x) \cos \frac{k_x}{2} + \eta(t+t_y) \cos \frac{k_y}{2} \right]^2 + \left[(t-t_x) \sin \frac{k_x}{2} - \eta(t-t_y) \sin \frac{k_y}{2} \right]^2} \\ &\equiv \pm |\varepsilon_\eta(\mathbf{k})|. \end{aligned} \quad (\text{S1.5})$$

We have defined that

$$\varepsilon_\eta(\mathbf{k}) \equiv t e^{ip_x} + t_x e^{-ip_x} + \eta [t e^{-ip_y} + t_y e^{ip_y}], \quad p_x \equiv \frac{k_x}{2}, p_y \equiv \frac{k_y}{2}. \quad (\text{S1.6})$$

Then, the eigen states for $h_A(\mathbf{k})$ then can be simply written as

$$\psi_\eta^A = \frac{1}{\sqrt{2}} \begin{pmatrix} 1 \\ \eta e^{-i\frac{k_x+k_y}{2}} \end{pmatrix}.$$

For the operator $h_B(\mathbf{k})$, we obtain

$$h_B(\mathbf{k}) = h_0(\mathbf{k})\sigma_0 + h_1(\mathbf{k}) \begin{pmatrix} 0 & e^{i\frac{k_y-k_x}{2}} \\ e^{-i\frac{k_y-k_x}{2}} & 0 \end{pmatrix}.$$

Then, the corresponding eigen states for $h_B(\mathbf{k})$ can be written as

$$\psi_\eta^B = \frac{1}{\sqrt{2}} \begin{pmatrix} 1 \\ \eta e^{-i\frac{k_y-k_x}{2}} \end{pmatrix}.$$

Therefore, the total wave function for $H(\mathbf{k})$ is

$$\Psi_\eta^\pm = \frac{1}{\sqrt{2}} \begin{pmatrix} \psi_\eta^A \\ \pm \psi_\eta^B \end{pmatrix} = \frac{1}{2} \begin{pmatrix} 1 \\ \eta e^{-i(p_x+p_y)} \\ \pm 1 \\ \pm \eta e^{-i(p_y-p_x)} \end{pmatrix}. \quad (\text{S1.7})$$

C. Dirac points

Due to chiral symmetry, the conduction bands and valence bands touch at $E = 0$. For the general case $t_x \neq t_y$, it requires the constraint $|\varepsilon_\eta(\mathbf{k})| = 0$ to have Dirac points, which implies the conditions

$$\begin{aligned} (t-t_x) \sin p_x + \eta(t-t_y) \sin p_y &= 0, \\ (t+t_x) \cos p_x - \eta(t+t_y) \cos p_y &= 0. \end{aligned}$$

We can further simplify these equations as

$$\cos^2 p_x = \frac{(t+t_y)^2(2t-t_x-t_y)}{4t(t^2-t_x t_y)}, \quad (\text{S1.8})$$

$$\cos^2 p_y = \frac{(t+t_x)^2(2t-t_x-t_y)}{4t(t^2-t_x t_y)}. \quad (\text{S1.9})$$

Therefore, by these two equations, we can identify the locations of the Dirac point at $\mathbf{K}_\pm = \pm(K_x, -K_y)$ with

$$K_x = 2 \arccos \sqrt{\frac{(t+t_y)^2(2t-t_x-t_y)}{4t(t^2-t_x t_y)}}, \quad (\text{S1.10})$$

$$K_y = 2 \arccos \sqrt{\frac{(t+t_x)^2(2t-t_x-t_y)}{4t(t^2-t_x t_y)}}. \quad (\text{S1.11})$$

D. Two-band effective model close to the Dirac points

At the Dirac points, the bands touch at zero energy. Let us first rewrite the Hamiltonian as

$$H(\mathbf{k}) = \begin{pmatrix} 0 & q(\mathbf{k}) \\ q^\dagger(\mathbf{k}) & 0 \end{pmatrix}; \quad q(\mathbf{k}) = \begin{pmatrix} e^{ip_x} z & e^{ip_y} w \\ e^{-ip_y} w & e^{-ip_x} z \end{pmatrix}, \quad (\text{S1.12})$$

where $z \equiv te^{ip_x} + t_x e^{-ip_x}$, and $w \equiv te^{-ip_y} + t_y e^{ip_y}$. We note that $\varepsilon_\eta(\mathbf{k}) = z + \eta w$. Let us focus on the point $\mathbf{K} = \mathbf{K}_+$. It is found that $\varepsilon_{\eta=-1}(\mathbf{K}) = z - w = 0$. Thus the Hamiltonian will be simplified to

$$H(\mathbf{K}) = \begin{pmatrix} & q(\mathbf{K}) \\ q^\dagger(\mathbf{K}) & \end{pmatrix}, \quad q(\mathbf{K}) \equiv z(\mathbf{K}) \begin{pmatrix} e^{iP_x} & e^{iP_y} \\ e^{-iP_y} & e^{-iP_x} \end{pmatrix}. \quad (\text{S1.13})$$

Then, we can find

$$h_A(\mathbf{K}) = q(\mathbf{K})q^\dagger(\mathbf{K}) = 2|z(\mathbf{K})|^2 \begin{pmatrix} 1 & e^{i(P_x+P_y)} \\ e^{-i(P_x+P_y)} & 1 \end{pmatrix}, \quad (\text{S1.14})$$

where $P_{x/y} \equiv \frac{K_{x/y}}{2}$. This Hamiltonian has a zero energy eigen value and with corresponding eigen state

$$\psi^A(\mathbf{K}) = \frac{1}{\sqrt{2}} \begin{pmatrix} 1 \\ -e^{-i(P_x+P_y)} \end{pmatrix}. \quad (\text{S1.15})$$

Similarly,

$$h_B(\mathbf{K}) = q^\dagger(\mathbf{K})q(\mathbf{K}) = 2|z(\mathbf{K})|^2 \begin{pmatrix} 1 & e^{-iP_x+iP_y} \\ e^{iP_x-iP_y} & 1 \end{pmatrix}. \quad (\text{S1.16})$$

This Hamiltonian also has a zero energy eigen value and with corresponding eigen states

$$\psi^B(\mathbf{K}) = \begin{pmatrix} 1 \\ -e^{i(P_x-P_y)} \end{pmatrix}. \quad (\text{S1.17})$$

Thus, the two eigen states with zero energy at \mathbf{K} are

$$\Psi_1(\mathbf{K}) = \frac{1}{\sqrt{2}} \begin{pmatrix} 1 \\ -e^{-i(P_x+P_y)} \\ 0 \\ 0 \end{pmatrix}, \quad \Psi_2(\mathbf{K}) = \frac{1}{\sqrt{2}} \begin{pmatrix} 0 \\ 0 \\ 1 \\ -e^{i(P_x-P_y)} \end{pmatrix}. \quad (\text{S1.18})$$

By Taylor expansion of the Hamiltonian near the \mathbf{K} points, we have

$$H(\mathbf{k}) = H_0(\mathbf{K}) + H'(\kappa), \quad (\text{S1.19})$$

$$H_0(\mathbf{K}) = \begin{pmatrix} 0 & 0 & t_x + te^{iK_x} & t + t_y e^{iK_y} \\ 0 & 0 & t_y + te^{-iK_y} & t + t_x e^{-iK_x} \\ t_x + te^{-iK_x} & t_y + te^{+iK_y} & 0 & 0 \\ t + t_y e^{-iK_y} & t + t_x e^{+iK_x} & 0 & 0 \end{pmatrix},$$

$$H'(\kappa) = i \begin{pmatrix} 0 & 0 & te^{iK_x} \kappa_x & t_y e^{iK_y} \kappa_y \\ 0 & 0 & -te^{-iK_y} \kappa_y & -t_x e^{-iK_x} \kappa_x \\ -te^{-iK_x} \kappa_x & te^{iK_y} \kappa_y & 0 & 0 \\ -t_y e^{-iK_y} \kappa_y & t_x e^{iK_x} \kappa_x & 0 & 0 \end{pmatrix},$$

where $\kappa \equiv \mathbf{k} - \mathbf{K}$. By the projection method, the effective Hamiltonian near the Dirac point can be written as

$$H_{\text{eff}}(\kappa) = \begin{pmatrix} \langle \Psi_1(\mathbf{K}) | H'(\kappa) | \Psi_1(\mathbf{K}) \rangle & \langle \Psi_1(\mathbf{K}) | H'(\kappa) | \Psi_2(\mathbf{K}) \rangle \\ \langle \Psi_2(\mathbf{K}) | H'(\kappa) | \Psi_1(\mathbf{K}) \rangle & \langle \Psi_2(\mathbf{K}) | H'(\kappa) | \Psi_2(\mathbf{K}) \rangle \end{pmatrix}. \quad (\text{S1.20})$$

Explicitly, we obtain

$$H_{\text{eff}}(\kappa) = \begin{pmatrix} 0 & \frac{i}{2} e^{iP_x} [\kappa_x (te^{iP_x} - t_x e^{-iP_x}) + \kappa_y (te^{-iP_y} - t_y e^{iP_y})] \\ h.c. & 0 \end{pmatrix}. \quad (\text{S1.21})$$

Simplifying it further, this leads to

$$H_{\text{eff}}(\kappa) = \mathbf{v}_1 \cdot \kappa \sigma_x + \mathbf{v}_2 \cdot \kappa \sigma_y, \quad (\text{S1.22})$$

where

$$\mathbf{v}_1 = \frac{1}{2} (-t \sin(2P_x), \quad -t \sin(P_x - P_y) + t_y \cos(P_x + P_y)), \quad (\text{S1.23})$$

$$\mathbf{v}_2 = \frac{1}{2} (-t \cos(2P_x) + t_x, \quad -t \cos(P_x - P_y) + t_y \cos(P_x + P_y)). \quad (\text{S1.24})$$

E. Topological charge

The Dirac point is characterized by a topological charge $Q_{\mathbf{K}_{\pm}}$ that can be calculated with the formula

$$Q_{\mathbf{K}_{\pm}} = \frac{1}{2\pi i} \oint_{\ell} d\mathbf{k} \cdot \text{Tr} [q^{-1}(\mathbf{k}) \nabla_{\mathbf{k}} q(\mathbf{k})], \quad (\text{S1.25})$$

where the loop ℓ is chosen such that it encircles a single Dirac point \mathbf{K}_{\pm} . Explicitly, we derive

$$\nabla_{\mathbf{k}} q(\mathbf{k}) = i \begin{pmatrix} te^{ik_x} & 0 \\ 0 & -t_x e^{-ik_x} \end{pmatrix} \hat{e}_x + i \begin{pmatrix} 0 & t_y e^{ik_y} \\ -te^{-ik_y} & 0 \end{pmatrix} \hat{e}_y,$$

$$q^{-1}(\mathbf{k}) = \frac{1}{R(k_x, k_y)} \begin{pmatrix} t + t_x e^{-ik_x} & -(t + t_y e^{ik_y}) \\ -(t_y + te^{-ik_y}) & t_x + te^{ik_x} \end{pmatrix},$$

$$R(k_x, k_y) \equiv (te^{ip_x} + t_x e^{-ip_x})^2 - (te^{-ip_y} + t_y e^{ip_y})^2 = z^2 - w^2.$$

Then, we obtain

$$Q_{\mathbf{K}_{\pm}} = \frac{1}{2\pi} \oint_{\ell} dk_x \frac{e^{ik_x} t^2 - t_x^2 e^{-ik_x}}{R(k_x, k_y)} + \frac{1}{2\pi} \oint_{\ell} dk_y \frac{e^{-ik_y} t^2 - t_y^2 e^{ik_y}}{R(k_x, k_y)}. \quad (\text{S1.26})$$

We find that for any loop enclosing a single Dirac point, we get a nonzero topological charge $Q_{\mathbf{K}_{\pm}} = \pm 1$.

F. Space-time inversion symmetry

The 2D SSH model has several symmetries. Let us list them in the following. Time reversal symmetry $\mathcal{T} = K$ implies

$$\mathcal{T}H(\mathbf{k})\mathcal{T}^{-1} = H(-\mathbf{k}). \quad (\text{S1.27})$$

Chiral symmetry $\mathcal{C} = \tau_3\sigma_0$ implies

$$\mathcal{C}H(\mathbf{k})\mathcal{C}^{-1} = -H(\mathbf{k}). \quad (\text{S1.28})$$

Particle-hole symmetry $\mathcal{P} = \mathcal{C}K$ implies

$$\mathcal{P}H(\mathbf{k})\mathcal{P}^{-1} = -H(-\mathbf{k}). \quad (\text{S1.29})$$

Note that inversion symmetry (with the center of the unit cell as the inversion center) is missing due to the alternative dimerization along adjacent two lattice rows or columns. However, if we perform a glide operation (half-unit translation) followed by an inversion operation, then the system goes back to itself. We term this symmetry as ‘‘glide-inversion’’ symmetry. Explicitly, the glide-inversion symmetry is expressed as

$$\mathcal{G}_I^{x,y}H(\mathbf{k})[\mathcal{G}_I^{x,y}]^{-1} = H(-\mathbf{k}), \quad (\text{S1.30})$$

where $\mathcal{G}_I^{x,y} = I \times g_{x/y}$ with $I = \tau_0 \otimes \sigma_1$ being the inversion operator ($\sigma_{i=1,2,3}$ are Pauli matrices), $g_x = \tau_1 \otimes \begin{pmatrix} e^{ik_x} & 0 \\ 0 & 1 \end{pmatrix}$ and $g_y = \tau_1 \otimes \begin{pmatrix} 0 & e^{ik_y} \\ 1 & 0 \end{pmatrix}$ the half-unit translations along the x/y -direction, respectively. Thus, the space-time inversion operator is given by $\mathcal{S} = \mathcal{G}_I^{x,y}\mathcal{T} = \tau_0 \otimes \sigma_1 \times g_{x/y}\mathcal{K}$, which is a local operation in the momentum space. Correspondingly, the space-time inversion symmetry reads

$$\mathcal{S}H(\mathbf{k})\mathcal{S}^{-1} = H(\mathbf{k}), \quad \mathcal{S}^2 = 1. \quad (\text{S1.31})$$

G. Phase diagram

Our 2D SSH model experiences three different phases: (i) semimetal phase with Dirac points; (ii) nodal-line semimetal phase; (iii) weak topological insulators phase. Let us further specify the three phases below.

Phase (i): To obtain Dirac points, we consider the ranges of $\cos^2 p_x$ and $\cos^2 p_y$ as

$$0 < \frac{(t+t_y)^2(2t-t_x-t_y)}{4t(t^2-t_x t_y)} < 1, \quad (\text{S1.32})$$

$$0 < \frac{(t+t_x)^2(2t-t_x-t_y)}{4t(t^2-t_x t_y)} < 1. \quad (\text{S1.33})$$

The conditions $\cos^2 p_x > 0$ and $\cos^2 p_y > 0$ lead to the inequalities

$$(a) : \begin{cases} 2t - t_x - t_y > 0, \\ t^2 - t_x t_y > 0; \end{cases} \quad b) : \begin{cases} 2t - t_x - t_y < 0, \\ t^2 - t_x t_y < 0. \end{cases}$$

For the first case (a), if we further assume $t > |(t_x + t_y)/2|$, then

$$t^2 > \left(\frac{t_x + t_y}{2} \right)^2.$$

From the famous inequality that

$$\left(\frac{a+b}{2} \right)^2 \geq ab, \text{ for } \forall a, b,$$

the condition

$$t^2 > t_x t_y$$

is always satisfied. Otherwise, if $t < |(t_x + t_y)/2|$, the second condition $t^2 > t_x t_y$ is not always satisfied. For the second case (b), since $t > 0$, we need $(t_x + t_y)/2 > 0$. Therefore, the two conditions are not always compatible.

We further need

$$\frac{(t + t_y)^2(2t - t_x - t_y)}{4t(t^2 - t_x t_y)} < 1. \quad (\text{S1.34})$$

It can be proven that in the regime $2t > |t_x + t_y|$ we have $t^2 - t_x t_y > 0$ and $2t - (t_x + t_y) > 0$. The above condition is equivalent to

$$(t - t_y)^2(2t + t_x + t_y) > 0, \quad (\text{S1.35})$$

which is also naturally true in the region $2t > |t_x + t_y|$. Therefore, the semi-metallic phase with Dirac points appear for

$$2t > |t_x + t_y|. \quad (\text{S1.36})$$

Phase (ii): From the unique form of energy spectrum, it is clear that the system has a gapless nodal line at

$$k_x + k_y = 0, \text{ if } t_x = t_y \neq t. \quad (\text{S1.37})$$

The appearance of a gapless nodal line is due to an accidental mirror symmetry when $t_x = t_y$, as will be discussed later.

Phase (iii): The weak topological insulator phase appears in the region $|t_x + t_y| > 2t$ and $t_x \neq t_y$. The phase boundary between weak topological insulator and semimetal phase is located at $|t_x + t_y| = 2t$.

Appendix S2: Anisotropic Fermi velocity at Dirac points

The effective Fermi velocity v of the Dirac points in our model can also be manipulated by parameter modulations. The effective Fermi velocity plays a crucial role in characterizing the transport properties of Dirac states. Let us define an angle θ between the wave-vector \mathbf{k} and the $+\hat{k}_x$ axis. As shown in Fig. S1(a), the anisotropic Fermi velocity shows sinusoidal behavior with respect to the angle θ , consistent with elliptical Dirac cones in the two-band effective model around \mathbf{K}_\pm . As tuning t_x and t_y , the Fermi velocity in different directions θ may change substantially [Fig. S1(b)]. Interestingly, the velocities along different directions coincide when $t_x = -t_y \simeq \pm 0.3t$, which indicates that the Dirac cones become isotropic.

Appendix S3: Symmetry protection of the nodal-line metallic phase

In this section, we discuss the symmetry protection of the nodal-line metallic phase. We have shown in the main text that there is a gapless nodal line at $k_x + k_y = 0$ when $t_x = t_y$. Under this condition, the system has mirror symmetry along the direction $x + y = 0$. In momentum space, we thus transform to

$$MH(k_x, k_y)M^{-1} = H(-k_y, -k_x), \quad (\text{S3.1})$$

where the mirror operator is given by

$$M = \begin{pmatrix} 0 & 1 & 0 & 0 \\ 1 & 0 & 0 & 0 \\ 0 & 0 & 1 & 0 \\ 0 & 0 & 0 & 1 \end{pmatrix}. \quad (\text{S3.2})$$

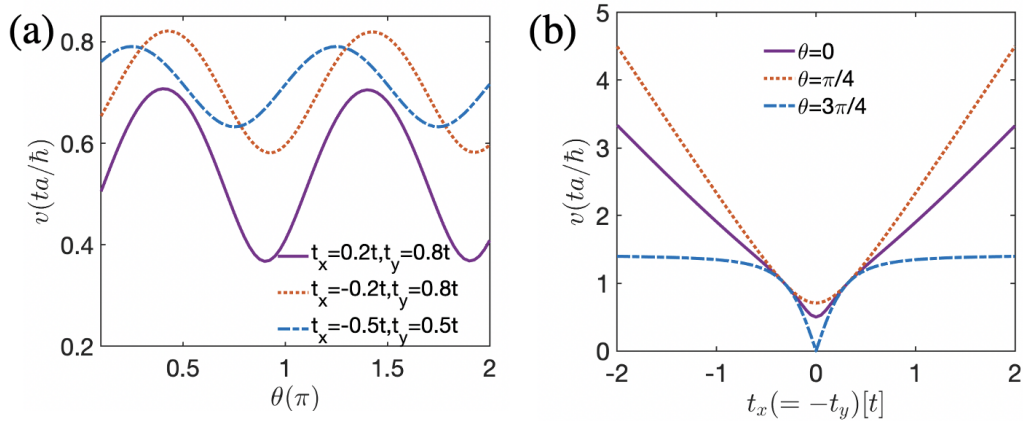


Figure S1. (a) Anisotropy of the Fermi velocity at the Dirac point \mathbf{K}_+ as a function of the angle θ for different t_x and t_y . Here, θ is defined as an angle between the wave-vector \mathbf{k} and $+\hat{k}_x$ axis. (b) Anisotropy of the Fermi velocity at the Dirac point \mathbf{K}_+ as a function of $t_x(=-t_y)$ for different angles θ .

Note that the Hamiltonian $H(\mathbf{k})$ commutes with the mirror operator M along the nodal-line $k_x + k_y = 0$. Therefore, we can label the eigen states of the Hamiltonian $H(\mathbf{k})$ by the eigen states of mirror operator M as

$$H(\mathbf{k})|\pm\rangle = \pm E|\pm\rangle, M|\pm\rangle = \pm|\pm\rangle. \quad (\text{S3.3})$$

We further note that the mirror operator commute with the chiral symmetry operator, i.e., $[\mathcal{C}, M] = 0$. Therefore, we can show that $\mathcal{C}|+\rangle$ is also an eigenstate of M with eigen value $+1$. Moreover, $\mathcal{C}|+\rangle$ is eigenstate of $H(\mathbf{k})$ with energy $+E$. Actually, the chiral symmetry maps the state $|+\rangle$ with energy $+E$ to state $\mathcal{C}|+\rangle$ with energy $-E$. This implies that those states are degenerated states at energy $E = 0$.

Appendix S4: Gap the Dirac points by perturbations

In this section, we discuss possible perturbation terms to gap the Dirac points. As we discussed in the main text, the stability of Dirac points is protected by space-time inversion symmetry. Indeed, if we add a staggered onsite potential, say $\Delta\tau_3\sigma_0$ with Δ indicating its strength, to break the glide-inversion symmetry, the Dirac points are removed and a bulk gap opens, as shown in Fig. S2(a). If we, however, consider another type of staggered onsite potential $\Delta\tau_0\sigma_3$, which breaks chiral symmetry, while it respects the glide-inversion symmetry, then the Dirac points remain intact (Fig. S2(b)).

Appendix S5: Graphene limit

In this section, we show that our 2D SSH model can reduce to graphene in a special limit. For instance, it is equivalent to a square lattice version of graphene when $t_x = t, t_y = 0$. In Fig. S3(a), the six sites in the dashed square resemble the hexagon in graphene. Therefore, when projecting the system to x -direction, the Dirac points are located at $(\pm\frac{2\pi}{3}, 0)$ [see Fig. S3(b)]. For the spectrum along perpendicular direction, there are no flat edge bands [see Fig. S3(c)]. Similar results are obtained if we consider the limit $t_x = 0, t_y = t$.

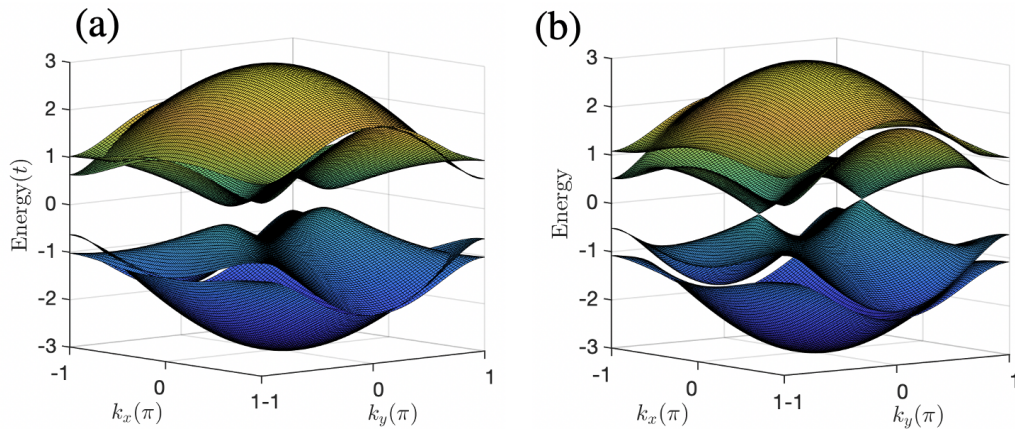


Figure S2. (a) Band structure of the 2D SSH model with a pair of Dirac points being gapped by $\Delta\tau_3\sigma_0$ with $\Delta = 0.1$. (b) Band structure of the 2D SSH model with a pair of Dirac points under the perturbation term $\Delta\tau_0\sigma_3$ with $\Delta = 0.1$. Other parameters are $t_x = 0.2t$ and $t_y = 0.8t$.

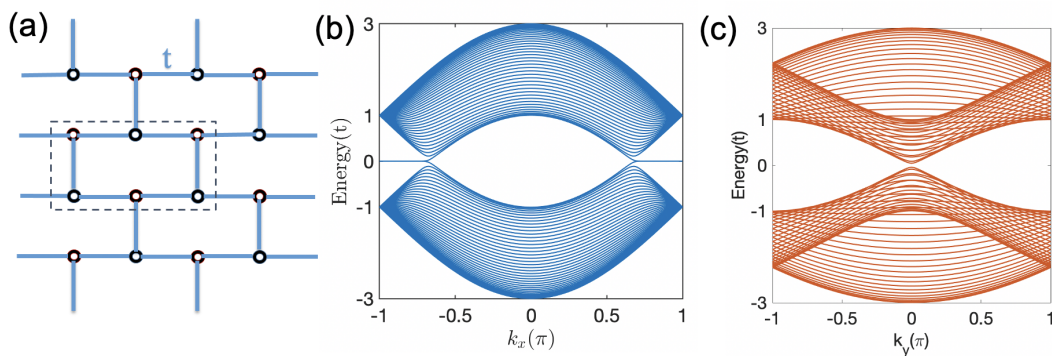


Figure S3. (a) Special limit of the our 2D SSH model with $t_x = t$ and $t_y = 0$. (b) Spectrum of ribbon with finite width $W_y = 20$ in the y -direction corresponds to panel (a). (c) Spectrum of ribbon with finite width $W_x = 20$ in the x -direction corresponds to panel (a). The spectrum in (b) and (c) are totally the same as the spectrum of graphene ribbon with zigzag and armchair edges, respectively.